PUBLICATION 4

Modeling of polymer electrolyte membrane fuel stack end plates

In: Journal of Fuel Cell Science and Technology 5(4),
art. no. 041009-1.

Modeling of Polymer Electrolyte Membrane Fuel Cell Stack End Plates

Suvi Karvonen
Laboratory of Advanced Energy Systems,
Helsinki University of Technology,
P.O. BOX 2200,
FIN-02015 TKK, Finland

Tero Hottinen
Wärtsilä Finland Oyj,
Tekniikantie 14,
02150 Espoo, Finland

Jari Ihonen

Heidi Uusalo

VTT Technical Research Centre of Finland,
P.O. Box 1601,
FI-02044 VTT, Finland

Good thermal and electric contacts of gas diffusion layers (GDLs) with electrode surface and flow-field plates are important for the performance of a polymer electrolyte membrane fuel cell (PEMFC). These contacts are dependent on the compression pressure applied on the GDL surface. The compression also affects the GDL porosity and permeability, and consequently has an impact on the mass transfer in the GDL. Thus, the compression pressure distribution on the GDL can have a significant effect on the performance and lifetime of a PEMFC stack. Typically, fuel cell stacks are assembled between two end plates, which function as the supporting structure for the unit cells. The rigidity of the stack end plates is crucial to the pressure distribution. In this work, the compression on the GDL with different end plate structures was studied with finite element modeling. The modeling results show that more uniform pressure distributions can be reached if ribbed-plate structures are used instead of the traditional flat plates. Two different materials, steel and aluminum, were compared as end plate materials. With a ribbed aluminum end plate structure and a certain clamping pressure distribution, it was possible to achieve nearly uniform pressure distribution within 10–15 bars. The modeling results were verified with pressure-sensitive film experiments.
[DOI: 10.1115/1.2930775]

Keywords: PEM fuel cell stack, end plates, compression, modeling

1 Introduction

The type of fuel cell under study in this paper is the polymer electrolyte membrane (a.k.a. proton exchange membrane) fuel cell, PEMFC. PEMFC is a low temperature fuel cell that typically operates in the temperature range of liquid water, although membranes that allow operation in higher temperatures have also been developed. PEMFCs are typically suitable for small-scale applications ranging from portable electronics to automobiles and distributed energy and heat production for houses and apartments. In order to make PEMFCs economically competitive and thus achieve large-scale fuel cell commercialization, the efficiency and lifetime of the cell must be maximized while the cost should be strongly reduced.

The operating voltage of a single PEMFC, less than 1 V, is low for most practical applications. Consequently, in a typical PEMFC power source, many cells are connected in series. Usually, the structure of PEMFCs is planar and thus the cells are stacked on top of each other; this arrangement is known as a fuel cell stack. Each unit cell in the stack has the following components: a solid electrolyte membrane and two electrodes that are usually integrated into a single component known as membrane electrode assembly (MEA), two gas diffusion layers (GDLs), two flow-field plates that can also be combined as a two-sided flow-field plate known as the bipolar plate, and insulation structures. The unit cells are inserted between end plates and the whole structure is fastened with a bolt assembly. A stack usually has also a cooling system so that the heat produced in the cells can be removed efficiently.

Good cell operation requires that the clamping pressure in each cell is approximately equal. The clamping pressure should also be distributed across the GDLs as evenly as possible since the attributes of the GDL are dependent on the compression pressure. The higher the pressure on the GDL is, the smaller are the thermal and electric contact resistances between the interfaces of the GDL with the electrode and flow-field plate. Typically, a compression pressure of 10 bars is sufficient for low contact losses as the contact resistances do not significantly decrease after that, see, e.g., Refs. [1,2]. On the other hand, high compression pressure decreases GDL porosity, which reduces its gas permeability and thus increases mass transfer limitations. As a consequence, the GDL porosity can have a significant effect on cell performance, see, e.g., Ref. [3]. The optimal pressure depends on the gas diffusion material and to some extent on cell operating parameters such as temperature or humidity of the inlet gases. Even pressures up to 30 bars on the rib area can be used for some materials [1]. However, as a compression of 10 bars is typically sufficient for contacts and excess compression causes mass transfer limitations, it is assumed here that a pressure distribution between 10 and 20 bars is sufficient, and 10 and 15 bars is ideal.

The local (under rib or channel) and regional (whole cell area) pressure distributions on the MEA and GDL are influenced by the dimensions, geometrical shape, and material of the stack components. The most important components in terms of the regional pressure distribution are usually the end plates, which should be as rigid as possible so that the clamping pressure of the bolt assembly that is typically located around the edges of the end plates is distributed across the whole cell area. From the manufacturing point of view, high rigidity is easily accomplished by making a simple thick flat plate. However, such a plate has large mass/volume, which results in a heavy/bulky stack. This is a serious disadvantage in most practical applications. Low mass and high rigidity can be simultaneously accomplished by using more complex end plate configurations such as ribbed structures. A ribbed structure is, in principle, a relatively thin flat plate with supporting ribs added to its surface. An interesting alternative to these high rigidity end plates is presented by curved shapes, more specifically curved end plates or additional curved layers inserted directly below the end plates such as described, e.g., in Ref. [4]. The curved component straightens when pressure is applied to the as-

Manuscript received October 31, 2006; final manuscript received October 19, 2007; published online September 9, 2008. Review conducted by Michael von Spakovsky.

sembly and thus produces an even pressure distribution if the original radius of curvature was suitably chosen for the used compression. However, this alternative requires high design and manufacturing accuracy in order to function properly. In this paper, the focus is on ribbed end plate structures.

The end plate material has a large influence on the mechanical properties of the end plate. A good end plate material has a high Young's modulus and a low density. Possible materials for end plates include, for example, steel, aluminum, and composite materials. In this work, two different materials, steel and aluminum, are compared. Steel has a high Young's modulus, typically approximately 200 GPa, but its density is also relatively high ($7600\ \mathrm{kg\,m^{-3}}$). Aluminum has a significantly lower Young's modulus, ~70 GPa, but on the other hand its density is also lower ($2700\ \mathrm{kg\,m^{-3}}$). If the end plate functions only as a supporting structure, other qualities such as corrosion characteristics or electric properties can be ignored, and the better choice of these two materials is the one that at a certain mass makes a more rigid end plate than the other one.

In this work, the stack assembly pressure distribution is studied using numerical analysis. The models were solved using a commercial partial differential equation solver, COMSOL MULTIPHYSICS® (formerly known as FEMLAB®) that employs the generally used finite element method (a.k.a. finite element analysis). The models made and solved in this work are based on the design of an existing fuel cell stack that is developed in the POWERPEMFC-project funded by the National Technology Agency of Finland (TEKES).

Earlier numerical studies on the pressure distribution and component deformation of a single cell have been made, e.g., by Lee et al. [5]. In their work, the modeled pressure distributions were clearly uneven so that the compression pressure on the middle area was significantly lower than on the edges. In this work, a significant improvement in the pressure distribution is accomplished by changing the plate structure from flat to ribbed plate. At the same time, the end plate mass is also significantly reduced.

2 Theory

The state of stress in an object is represented by the stress tensor σ as follows:

$$\sigma = \begin{bmatrix} \sigma_x & \tau_{xy} & \tau_{xz} \\ \tau_{xy} & \sigma_y & \tau_{yz} \\ \tau_{xz} & \tau_{yz} & \sigma_z \end{bmatrix} \tag{1}$$

which consists of the normal stresses σ_i and shear stresses τ_{ij}. Here, it is assumed that adjacent shear stresses are equal, $\tau_{ij}=\tau_{ji}$, which applies for most materials. For an object in equilibrium state with no volume forces acting on it, the stress tensor obeys the following differential equation, see, e.g., Ref. [6]:

$$\nabla \cdot \sigma = 0 \tag{2}$$

The stress tensor is often written in vector notation as $\sigma = (\sigma_x, \sigma_y, \sigma_z, \tau_{xy}, \tau_{yz}, \tau_{xz})^T$. With this formulation, the stress tensor in an elastic material can be calculated from the strain tensor $\varepsilon = (\varepsilon_x, \varepsilon_y, \varepsilon_z, \gamma_{xy}, \gamma_{yz}, \gamma_{xz})^T$ by Hooke's law as follows:

$$\sigma = D\varepsilon \tag{3}$$

where D is the elasticity matrix. Here, it is assumed that there are no initial stresses or strains that can occasionally be created during the manufacturing process in the materials. The elasticity matrix is calculated using Young's modulus E and Poisson's ratio ν as follows:

$$D = \frac{E}{(1+\nu)(1-2\nu)} \begin{bmatrix} 1-\nu & \nu & \nu & 0 & 0 & 0 \\ \nu & 1-\nu & \nu & 0 & 0 & 0 \\ \nu & \nu & 1-\nu & 0 & 0 & 0 \\ 0 & 0 & 0 & \frac{1}{2}-\nu & 0 & 0 \\ 0 & 0 & 0 & 0 & \frac{1}{2}-\nu & 0 \\ 0 & 0 & 0 & 0 & 0 & \frac{1}{2}-\nu \end{bmatrix} \tag{4}$$

The derivation of D can be found in many structural mechanics books, see, e.g., Ref. [7], and is thus not repeated here. In this work, all materials are approximated as elastic, isotropic, and homogeneous so that the material parameters E and ν are constant in each component. Thermal stresses due to a temperature difference caused by the heat production of the operating fuel cell are excluded since the operating temperature of the PEMFC is typically less than 373 K. Temperature differences within the unit cells are usually at largest 20 K, see, e.g., Ref. [8]. Some error is likely introduced to the modeled GDL pressure distributions due to the assumption of constant material parameters. In reality, the composite material of the flow-field plates is not isotropic and the elastic approximation is not entirely valid for some of the materials, such as the carbon paper of the GDLs. However, the approximations are valid for the metallic end plates that have the largest influence on the pressure distributions throughout the stack. Thus, the results given by the model should be good approximations of the real situation.

The strain ε is a measure of the material's deformation that is calculated by dividing the change in length at a certain point by the original length at that point. The components of the strain tensor ε are calculated from the deformation vector, $\mathbf{u}=u\mathbf{i}+v\mathbf{j}+w\mathbf{k}$, as follows:

$$\varepsilon_i = \frac{\partial \mathbf{u}_i}{\partial i} \tag{5}$$

$$\gamma_{ij} = \frac{\partial \mathbf{u}_j}{\partial i} + \frac{\partial \mathbf{u}_i}{\partial j} \tag{6}$$

Using these equations, the following differential equation can be written for the deformation:

$$\nabla \cdot (D\nabla \mathbf{u}) = 0 \tag{7}$$

This is the equation solved with COMSOL MULTIPHYSICS®. The solution consists of the deformation values, from which the stress and strain components can be calculated using Eqs. (3)–(6). The most interesting aspect of the results is the compression pressure on the GDL. It is taken as the z-directional stress component, i.e., σ_z. According to Eqs. (3)–(6), this can be calculated from the deformation components as

$$\sigma_z = \frac{E}{(1+\nu)(1-2\nu)} \left(\nu \frac{\partial u}{\partial x} + \nu \frac{\partial v}{\partial y} + (1-\nu) \frac{\partial w}{\partial z} \right) \tag{8}$$

3 Model Properties

The model geometry was based on an existing fuel cell stack design. However, solving a model that includes each geometrical detail was not possible with the available computing capacity. In order to restrict the number of elements in the models to a reasonable limit, the geometry was simplified by reducing the number of different components and approximating some of the more complex structures with simpler ones.

In the real stack design that was used as a basis for the models in this work, each unit cell consists of the following components:

- two 3 mm thick polymer composite flow-field plates
- two 1 mm thick layers including gasket material (Grafoil®),

Table 1 The values of Young's modulus and Poisson's ratio for the different components

	E (GPa)	υ	Source
Flow-field plate (graph/epoxy)	10	0.25	Estimate, material still in development
Gas diffusion layer	0.06	0.33	Taken the same as in Ref. [5]
Grafoil	1.4	0.25	[9]
Steel	200	0.33	Well known material
Aluminum	70	0.33	Well known material
Rubber	0.1	0.4	Estimate
Steel net	110	0.33	Estimate

gas space, and steel net (part of the gas distribution and cooling systems)
- one ~0.5 mm thick layer including two rubber gaskets for gases, two GDLs (SGL Sigracet 35 BC), and MEA
- one 0.5 mm thick metal (steel) separator plate

The total thickness of a unit cell is thus 9 mm. The cross-sectional area of the end plates and flow-field plates is 258×190 mm^2.

In the modeled stack, each cell was reduced to the following three homogeneous components:

- one 8.5 mm thick plate that includes the two 3 mm flow-field plates, the 0.5 mm metal plate, and the two 1 mm Grafoil® layers with the steel nets
- the two rubber gaskets merged into one component with a simplified geometry
- 0.5 mm layer that represents the two GDLs and MEA.

In addition to reducing the multitude of components to only three, the geometry was simplified by excluding fine geometrical details such as the flow-field pattern (1 mm wide gas channels crossing the cell) and the bolt holes with the bolts set through them. This simplification should be justifiable since the exceptions to symmetry in the flow-field pattern are relatively minor in terms of the cross-sectional area. The curved shape of the rubber insulator was approximated with a polygon. The two material parameters, E and υ, of the two latter components were simply those of rubber and the GDL material (Carbel®). The MEA is relatively thin and flexible so that the GDLs dominate the deformation of the GDL-MEA component. However, the material parameters of the 8.5 mm thick plate formed by many different materials could not be defined as easily. Thus, a separate model was solved to discover the proper values for this component. The rigidity of the flow-field plate–gasket–separator assembly was studied with this model, first with the real E and υ of each separate component and the detailed component geometry, and then with the constant values using the simplified geometry (homogeneous plate with gas and cooling system channels). The result was that with $E = 7.7$ GPa, the deformation behavior of the homogeneous plate was similar to the more detailed model. Poisson's ratio υ was taken as 0.25, since that was the value of all component materials except the relatively thin steel separator plate. The values for E and υ of the different materials are listed in Table 1 and cross-sectional schematics of the real stack and model components are presented in Fig. 1. The error induced by these approximations is studied in a separate section.

Since the channel configurations in the flow-field plates were excluded, the modeled fuel cell stack was a symmetric structure with respect to the center in all three dimensions. Thus, through employment of symmetry boundary conditions, it is sufficient to solve the problem in only one-eighth of the whole stack geometry. The model geometry consists of one-quarter of the cross-sectional area of the cell and one-half of the stack (three cells). On each symmetry boundary, the deformation in the direction normal to the surface is fixed to zero. A schematic of the modeled flat end plate and its symmetry axes are presented in Fig. 2. The compression is directed to the object by setting 1 kN load divided with the area of the used spring washers on each of the circular areas marked in Fig. 2. The bolt holes and the bolts set through them were not included in the models as separate geometrical objects since they complicate the mesh and do not significantly affect the rigidity of the end plates.

The original end plate, whose cross section is illustrated in Fig. 2, was a flat 2 cm thick steel plate that has a weight of 7.1 kg. The two objectives of this work were to lower the end plate mass and simultaneously improve the GDL pressure distribution. In this work, it is assumed that a sufficient GDL pressure distribution is restricted to between 10 and 20 bars, and only those end plate configurations that result in pressure distributions that obey this criterion were recognized as acceptable.

One method of lowering the end plate mass while increasing its rigidity is to reduce the thickness of the plate and then add supporting ribs in a suitable configuration to its surface. The resulting structure is known as a ribbed end plate. The rigidity of a rib with a square cross section is proportional to the third power of its height d but only directly proportional to its width b, see, e.g., Ref. 7:

$$I = \tfrac{1}{12} b d^3 \tag{9}$$

Thus, a high and thin rib will be more rigid than a low and wide one that has the same volume. In practice, the manufacturing process and the possible applications of the stack limit the dimensions of the ribs.

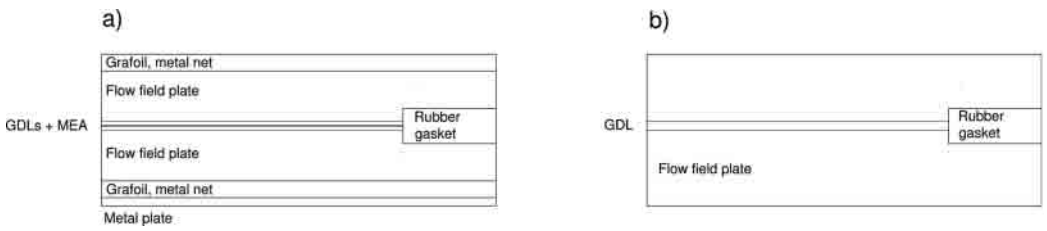

Fig. 1 A cross-sectional schematic of the unit cell components in (*a*) a real stack and (*b*) the approximative model

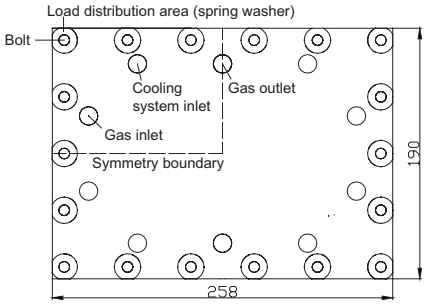

Fig. 2 A top (*x*,*y*-plane) view of the flat end plate structure. The dimensions are in millimeters.

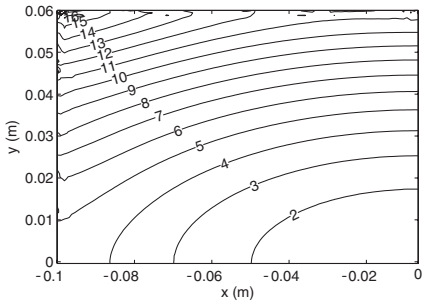

Fig. 4 The clamping pressure isobars on the GDL surface of the original flat plate with 1 kN load at each bolt. The pressure values are in bars. The origin (lower right corner) corresponds to the point of symmetry.

The geometric possibilities for the placement, thickness, and width of the ribs are infinite. However, the ribs cannot cross the gas and cooling system inlets and outlets. Furthermore, setting the ribs from one bolt to another improves the load distribution across the whole area, and thus the number of possible rib structures can be decreased to such geometries only. In this work, the search for the best geometry was limited to three alternative rib structures illustrated in Fig. 3. Modeling these structures revealed that Structure (*b*) in Fig. 3 was the most promising one. Structure (*a*) is the most simple to manufacture and has the lightest weight, but its pressure distribution is only slightly better than that of the original flat plate. Structure (*c*) has the best pressure distribution, but not significantly better than Structure (*b*). Therefore, because Structure (*c*) is clearly heavier than Structure (*b*), the latter would appear to be the most advantageous choice and was accordingly chosen for further study. Different rib widths and heights were tested with both steel and aluminum and the results for the best structures are presented in the next chapter.

The geometry was meshed with tetrahedral elements. Because the GDL-MEA component is very thin compared to its length and width, the mesh elements were flattened in the *z*-direction. The used values for the scaling factor, i.e., the height of the normal element divided by the height of flattened element, varied between 2.5 and 3.5. This mesh manipulation reduced the number of elements from 300,000 to 70,000–95,000 elements depending on the geometry. When different scaling factors between 2 and 4 were tested, the differences between the corresponding GDL pressure distributions were in the range of 2% and this is likely due more to the differences in the total number of elements than the scaling. Thus, scaling the mesh should not affect the results significantly. The calculations were performed over a 64 bit COMSOL MULTIPHYSICS® client-server connection. The server computer was an AMD Athlon64 3500+ with 4 Gbyte random access memory (RAM) and 40 Gbytes of swap space. The operating system was SuSe 9.1 AMD64 Linux. With this equipment, a model was usually solved in a few hours.

4 Results

The pressure distribution data were taken from the middle (in *z*-direction) of the GDLs. Unless mentioned otherwise, the results were taken from the second cell from the end plates. The results for the flat end plate with constant 1 kN point loads are illustrated in Fig. 4. The compression pressure isobars are curved and the largest pressure, approximately 16 bars, is found in the left upper corner that corresponds to the four outer corners of the GDL. In contrast, at the lower right corner, i.e., the middle area of the GDL, the pressure values are much lower, close to 1 bar. The pressure map illustrated in Fig. 4 represents the average pressure values over several channel widths. The disturbances on the top and left edges are caused by contact of the GDL with the rubber gasket at the interface boundaries, where the deformation of the rubber affects the stresses in the GDL. The pressure values are more easily read from Fig. 5, where the values are taken along the diagonal of the GDL (from upper left corner to lower right corner in Fig. 4).

If the disturbances close to the rubber gasket–GDL interface are ignored, the pressure distribution is a monotonous function as can be seen from Fig. 5. The compression pressure is at maximum in the outer corner of the GDL. This is in accordance with previous results such as those presented by Lee et al. [5]. The maximum and minimum pressures are 16.5 bars and 1.1 bars, respectively. The compression pressure at the middle regions of the GDL is very small, than 2 bars, and only 6.7% of the pressure at the outer corner, whereas optimal cell performance can be assumed to require at least 10 bars and a significantly more homogeneous pressure distribution. Smaller pressures are likely to cause high thermal and electric contact resistances, which decrease the cell performance and can cause heat removal problems, which can significantly shorten the lifetime of the cell. These results suggest that significant improvement in cell performance could be achieved if the unsatisfactory GDL pressure distribution could be made more even by modifying the end plate structure.

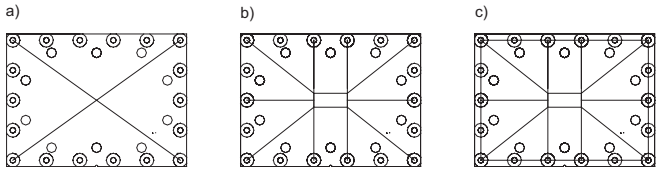

Fig. 3 Schematic representations of three different rib structures: (*a*) the two-rib, (*b*) the ten-rib, and (*c*) the edge-supported ten-rib structures.

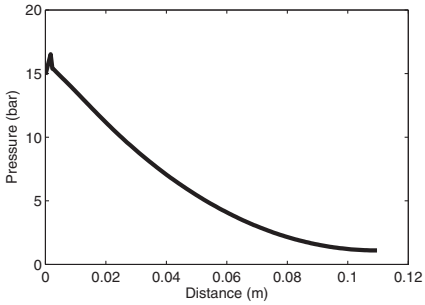

Fig. 5 The diagonal GDL pressure values of the flat plate structure with 1 kN load at each bolt

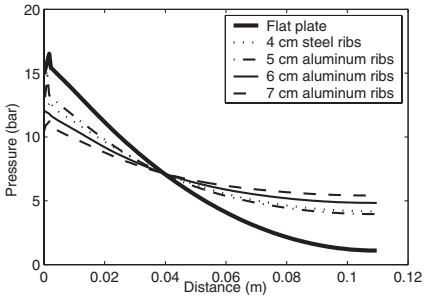

Fig. 7 The diagonal GDL pressure values of the studied steel and aluminum structures with 1 kN load at each bolt

As mentioned in Sec. 3, the best structure of the choices considered here is the ten-rib structure illustrated in Fig. 3(*b*). This structure was tested with both steel and aluminum. Steel has a larger Young's modulus than aluminum (see Table 1), which makes steel structures more rigid. On the other hand, aluminum is much lighter than steel and thus larger amounts of aluminum can be used without the end plate mass growing too large. The cross sections of the ten-rib structures used with steel and aluminum are illustrated in Fig. 6. The difference between the two structures is that the aluminum bars are wider and higher than those of the steel structure since aluminum is less rigid and has a lighter density. Note that the ten-rib configurations used here are not necessarily the optimal ones, but ones that were found to be sufficiently rigid for use in the stack studied in this work.

The GDL pressure distribution results for the steel and aluminum ten-rib structures are illustrated in Fig. 7. These data show that the best result, i.e., the most even GDL pressure distribution, is achieved with 7 cm high aluminum ribs. Nevertheless, the pressure distributions achieved with the other structures are also significantly better than that of the original flat steel plate. The most uneven compression is achieved with the 5 cm high aluminum ribs and the 4 cm high steel ribs. If higher or wider steel ribs were made, a better distribution would be gained, but this would increase the end plate mass over the original 7.1 kg limit. The pressure isobars of the best structure, the 7 cm aluminum rib structure, are illustrated in Fig. 8. The shape of the isobars has changed from the nearly elliptical ones of the flat plate in Fig. 4 closer to linear.

None of the pressure distribution curves presented in Fig. 7 is in the desired 10–20 bar range. This is due to the fact that the 1 kN load at each bolt is insufficient. For this reason, the loads were increased. Another consideration is that using the same load at each bolt does not give an optimal pressure distribution. This can be seen also in Fig. 8, where the shape of the pressure isobars suggests that the loads at the bolts at the middle of the edges are too small compared to the loads at the corner bolts. Increasing the loads at the middle of the edges and decreasing them at the corners should flatten the GDL pressure distribution. Different loads were tested through a trial-and-error method until the desired GDL pressure range was achieved. The shape of the pressure isobars was also monitored. Ideally, the isobars should be rectangular.

The results accomplished with bolt load variation are illustrated in Fig. 9. The 7 cm aluminum structure gives the best results with 10–15 bar GDL pressure range and the original objective; 10–20 bar is satisfied with the 4 cm steel and 5 cm aluminum structures. The GDL pressure isobars of the different structures are presented in Fig. 10. Unlike in Fig. 8 with the constant 1 kN bolt load, the pressure isobars are no longer close to linear. Instead, the curves loosely follow the rectangular shape of the GDL. Comparison of Figs. 10(*a*)–10(*d*) confirms that the 7 cm aluminum rib structure has the most even GDL pressure distribution.

It should be noted that the pressure distributions in the different cells of the stack have some differences. The GDLs of the cells closest to the end plates have the most uneven pressure distribution while the GDLs of the cells in the middle of the stack experience compression more evenly. This effect is illustrated in Fig. 11, where the pressure distributions in three cells with 7 cm aluminum rib end plate can be compared to each other.

The masses of the different structures are listed in Table 2 along with the corresponding GDL pressure ranges. As can be seen in Table 2, the 7 cm aluminum structure that had the best pressure distributions weighs 3.7 kg, whereas the 4 cm steel structure weighs 6.5 kg. Consequently, from the mechanical point of view, aluminum would seem to be the better choice as a material despite its lower Young's modulus. However, it is not yet clear which of the aluminum structures should be chosen for a real stack since it

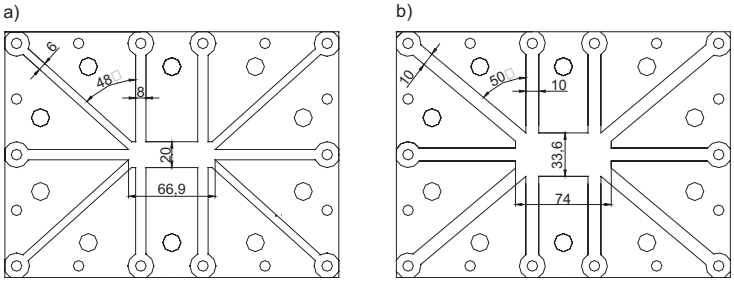

Fig. 6 A schematic of the ten-rib structures for (*a*) steel and (*b*) aluminum. The dimensions are in millimeters.

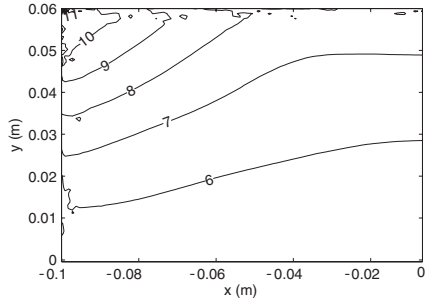

Fig. 8 The clamping pressure isobars on the GDL surface of the 7 cm aluminum rib structure with 1 kN load at each bolt. The pressure values are in bars.

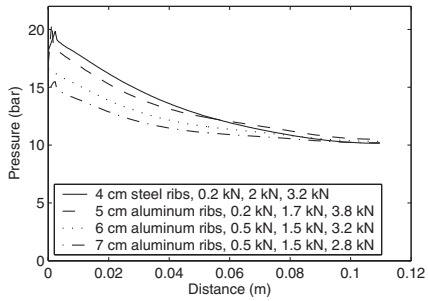

Fig. 9 The diagonal GDL pressure values of the structures with optimized bolt loads. The first load value refers to the corner bolt, the second to the bolts next to the corner, and the last to the bolts at the middle of the edges.

is not known whether there is any significant difference in the fuel cell performance if the GDL pressure distribution is 10–15 bars instead of 10–20 bars. If no difference can be experimentally observed, then the 0.7 kg lighter 5 cm high rib structure can be chosen instead of the 7 cm high structure. In large stacks that consist of many unit cells, the weight difference may be negligible, since the weight of the unit cells used in these experiments is approximately 0.9 kg and stacking 100 or more cells makes the reduction in end plate weight negligible. However, some mobile low voltage applications require stacks with only a few cells that have large areas. In these stacks, the rigidity of the end plates is crucial and the weight of the end plates becomes a significant factor.

5 Error Estimation

The effect of the mesh was studied with the flat plate model that usually had approximately 64,000 elements. This model was solved using three different meshes: 74,000, 80,000, and 95,000, and the pressure distributions were compared. The maximum differences in the GDL pressure values between the solutions given by the original mesh and larger meshes were below 1.5%. The relative errors are largest at the middle area of the cell, where the compression pressure is small. In order to check that each of the models presented in this work gives reliable results, each model was solved with two different meshes. The maximum differences between the solutions varied in the range of 1–3%, so the error induced by the mesh can be considered insignificant.

To further simplify the model, the flow-field plates, gasket layers, and metal nets were replaced with a single homogeneous component as described in Sec. 3. The value for the Young's modulus of this approximative component was taken as the value that resulted in a similar deformation of the homogenous component compared to that of the combined original components as determined with a separate model, i.e., 7.7 GPa. However, some error is likely introduced to the models because of this simplification. Therefore, the flat plate model was solved with two different Young's moduli, 5 GPa and 10 GPa, for the homogeneous component. The larger value, 10 GPa, corresponds to the Young's modulus of the flow-field plates. Despite the significant difference (over 30%) in the Young's modulus of the homogeneous plate, the

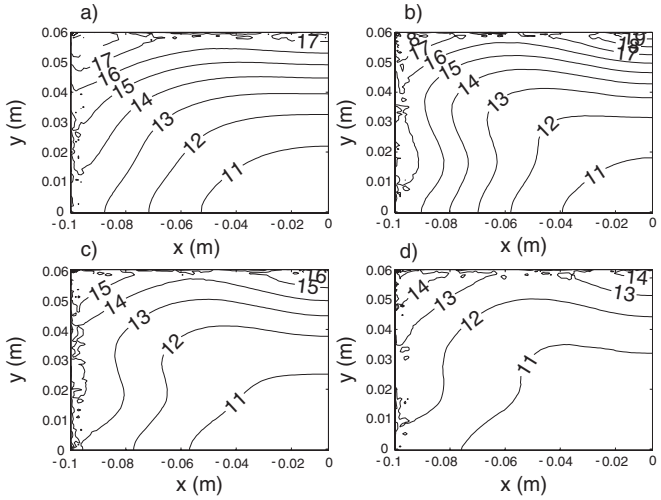

Fig. 10 Pressure isobars on the GDL: (*a*) 4 cm steel ribs, (*b*) 5 cm aluminum ribs, (*c*) 6 cm aluminum ribs, and (*d*) 7 cm aluminum ribs. The pressure values are in bars.

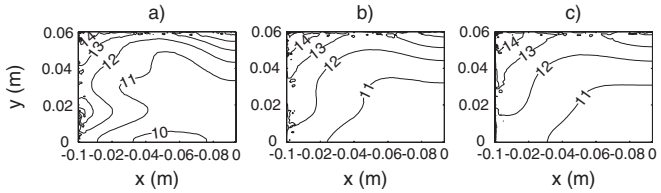

Fig. 11 The pressure isobars of the 7 cm aluminum ribs on the three GDL surfaces: (*a*) top (outermost), (*b*) middle, and (*c*) bottom (closest to *z*-symmetry boundary, i.e., middle of the stack)

compression values are close to similar. The relative differences are largest at the middle region of the cell where the pressure values are small at 7% with 10 GPa and 18% with 5 GPa data. Thus, it can be assumed that approximating the different components with a single homogeneous one should not give rise to an unacceptable source of error.

The models include other sources of inaccuracy besides the mesh and the reduced number of components discussed above. The material values for some of the components such as the flow-field plates and the GDL were only estimates of the real values. It is also probable that the Young's moduli for these components are, in fact, dependent on the stress in the material and not constant as assumed in the modeling. Also, several fine details of the cell structure were excluded to decrease the number of degrees of freedom. However, the stress and strain behavior of the stack is dominated by the end plates and their properties are known with good accuracy. The effect of the fine geometrical details is very local and uninteresting for end plate development. Furthermore, even though the compression data might not be exact, comparison of the data achieved with different end plates should still give valid information on which end plate structure is the most promising one.

6 Experiment

The modeling results were verified with experiments. Two of the modeled end plate structures, the original flat plate and the 5 cm rib aluminum plate, were manufactured and compared experimentally. Experiments were made with both a five-cell stack assembly and a unit cell assembly where the MEAs were replaced with a Pressurex® Super Low pressure-sensitive film. The advantage of the latter was that there was much less noise in the measurements, which will be discussed in more detail later in this section. It should be noted that neither of the experimental results corresponds exactly to the modeled situation (i.e., a six-cell stack), which was due to practical considerations of available materials. However, not only is there not much difference in practice between a five- and a six-cell stack, but also the essential point in these experiments is not to get the exact same pressure distributions as modeled but rather to be able to verify the advantageousness of the optimized structure in general. In addition, it was noticed in the experiments that quantitative validation was in any case impracticable with the available measurement accuracy, which is to be discussed in more detail later in this section.

Prior to the stack pressure measurements, the relationship between the color intensity of the film and the clamping pressure directed to the film was studied with calibration measurements. However, later experiments showed that despite the measurements being done in controlled ambient temperature and humidity, even the films corresponding to different cells in the stack had varying total color intensity levels, even though the pressure in each cell was definitely the same. A possible reason for this behavior is inhomogeneous quality of the pressure-sensitive film. Thus, the actual pressure values given as results of each measurement are not reliable. However, the differences in intensity, i.e., pressure, on each pressure-sensitive film, should not be strongly affected and thus results from different experiments can be compared to each other, not through the actual pressure but rather through the variation in pressure.

In each measurement, the stack was assembled with all components, excluding the MEAs, which were replaced with pressure-sensitive films. The metal net was replaced with Grafoil® because the thickness of the available metal net was significantly different from the surrounding Grafoil® gasket, which would have led to disturbances in the pressure distribution. The bolts were tightened gradually to avoid inhomogeneous compression on the stack at any time during the assembly. The compression in the assembled stack was let to stabilize. After disassembly, the pressure-sensitive films were scanned. The color intensity values were changed into pressure values by using the calibration data and compared to the average pressure measured by each film. Finally, the pressure data were averaged over the four symmetrical cell segments in order to minimize the effect of thickness variation in the stack components. The pressure values were also smoothed by local averaging so that the uninteresting effect of the channel structure was mostly lost and the pressure distributions became easier to compare to the modeling results.

The largest single source of error in these measurements was, however, the manufacturing tolerance of the different cell components, e.g., in flow-field plates the thickness variation was on average 0.1 mm and at maximum 0.15 mm. This error was to some extent mitigated by pairing off the flow-field plates so that the manufacturing defects in the two plates canceled each other out. Nevertheless, this method of increasing the accuracy was relatively unsophisticated and the measurement results clearly show the effect of the thickness variation. The noise from this effect was so significant that stack experiments with the optimized clamping pressures, which had been originally planned, were not performed at all since the pressure distribution measured with the optimized end plate was so uniform that any differences were almost inseparable from the noise. This is why the unit cell measurements were

Table 2 The masses and achieved pressure ranges of the different structures

Component	Mass (kg)	Mass/mass of flat plate (%)	Pressure range (bar)
4 cm steel ribs	6.5	92	10–20
5 cm aluminum ribs	3.0	42	10–20
6 cm aluminum ribs	3.4	47	10–17
7 cm aluminum ribs	3.7	52	10–15

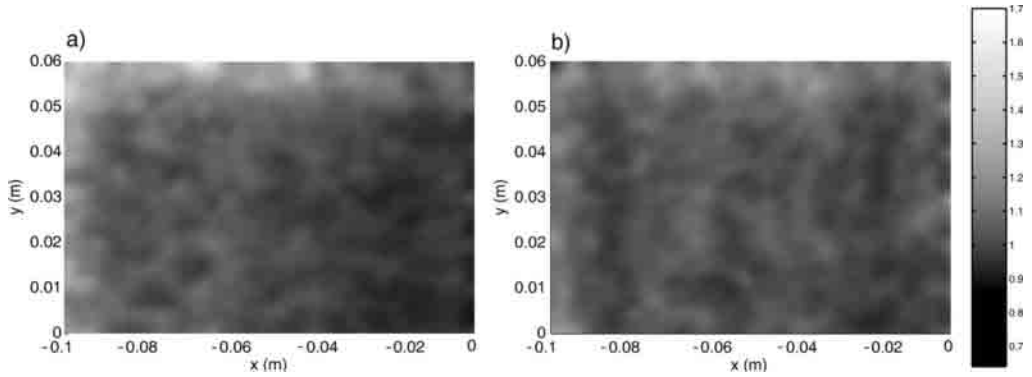

Fig. 12 The five-cell stack measurement results: (*a*) corresponds to the pressure on the middle cell in the stack with the original flat end plates and (*b*) to the 6 cm rib aluminum plates. The color bar values show the pressure value in relation to the average clamping pressure.

also performed; with far fewer components, there is also less noise present in the results and the improvement in the pressure distribution that can be had by using the optimized clamping pressures could be seen.

The results from the five-cell stack measurements are illustrated in Fig. 12. While in Fig. 12(*a*) the pressure is clearly smaller in the middle, as predicted by the modeling, in Fig. 12(*b*) the background noise is dominating the pressure distribution. The results from the single cell measurements are illustrated in Fig. 13. Here, the distorting noise is smaller and the pressure distribution is closer to the one predicted by the modeling. It should be noted that in Fig. 13(*a*), the pressure values in the lower right corner corresponding to the center of the cell are too large. This is due to the fact that the used pressure-sensitive film does not show pressures beneath 6.5 bars, which corresponds to the minimum relative pressures shown in these pictures. Taking this into consideration, it is clear that the pressure distribution measured with the 6 cm aluminum rib end plates is clearly more homogeneous than that of the original flat plate. With the single cell experiments, it was also possible to study the effect of using the optimized clamping pressures. The measurement results are shown in Fig. 13(*c*), where the pressure distribution is clearly more even than in the two other cases. The reason for the low pressure values on the right edge of the figures is the flow-field plate channel structure.

7 Summary and Discussion

The compression pressure distribution on the GDLs in a PEMFC stack was studied by modeling using the finite element method. The results show that the often used flat steel plate structure is not only heavy and thus impractical for many applications, but also clearly inferior in terms of the GDL pressure distribution to alternative structures such as a ribbed aluminum plate. Thus, even though aluminum has a lower Young's modulus than steel, it is nevertheless the better choice for an end plate in terms of the end plate mass since its density is also lower. The GDL compression pressure directly affects the electric and heat contact resistances between the GDL and the flow-field plates and the MEA as well as the GDL mass transport properties and consequently the GDL pressure distribution can be assumed to affect the performance and lifetime of the cell.

Using the aluminum rib structure with optimized clamping pressure at each bolt, it was possible to improve the 1–17 bar pressure distribution corresponding to the original flat plate to 10–15 bars with the aluminum rib structure. At the same time, the end plate mass was reduced to half of the original. It would seem that a pressure range of 10–15 bars or 20 bars is ideal so that the contact resistances are low enough while GDL is not compressed too heavily for the mass transport properties to suffer significantly.

In the modeling, all component materials were assumed to be elastic and the cell structure was simplified by reducing the number of components and excluding details such as the flow-field channel structure. As a result of these idealizations and the fact that in reality the stack components are not uniform in thickness due to manufacturing tolerances, the model results were not expected to exactly correspond to experimental data.

The improvement in the pressure distribution range is significant, since a compression in the range of a few bars as in the original case is so low that the contact resistances can be expected

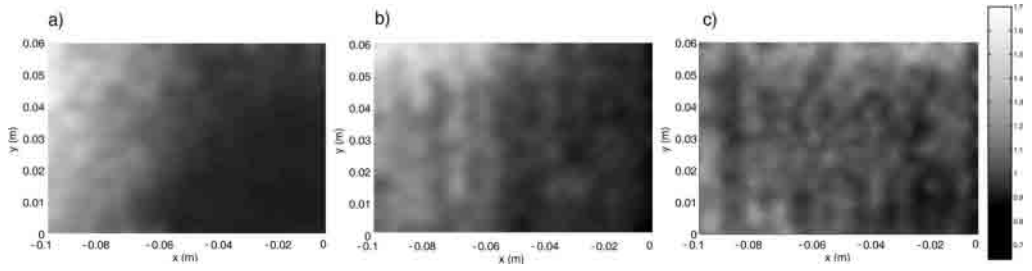

Fig. 13 The single cell measurement results: (*a*) original flat plates with homogeneous clamping, (*b*) 6 cm rib aluminum plates with homogeneous clamping, and (*c*) 6 cm rib aluminum plates with optimized clamping distribution. The color bar values show the pressure value in relation to the average clamping pressure.

to be too high for good performance. Experimental study of the modeled end plate structures did not show quite as much improvement, which was to large degree due to manufacturing defects, i.e., significant thickness variation in the cell components. However, in five-cell stack experiments, the aluminum rib structure proved to have a more even pressure distribution. In the stack experiments, the noise due to the thickness variations was so large that studying the effect of optimizing clamping pressure was not practicable. Consequently, this was studied with a single cell assembly, where the difference was easier to see and, as expected according to the modeling results, the pressure distribution was improved by optimizing the clamping pressure.

In a stack, the compression differences between end cells and middle cells are unavoidable. The more uneven pressure distribution in end cells can lead to reduced gas flows, which usually results in increased flooding. By using simulations, it can be estimated whether the difference between the middle cells and end cells will lead to major deviation in performance that can be called "end cell problem."

The experiments also showed that in many cases, inadequate tolerances in the thickness of the cell components can be a significant problem. In the experiments performed in this work, the flow-field plates were arranged so that the thickness variation was to some extent canceled. However, a random arrangement when components with low tolerances are used is likely to lead to a worse scenario, where the GDL compression is much larger on one side of the cell than on the other. Interestingly, the problem is quite different in a single cell assembly, where the problem is more that there is not enough noise to smooth the pressure distribution and thus the end plate design becomes more critical, which incidentally is quite the opposite to the usual phenomenon of problems increasing when moving from unit cells to stacks. It would also seem that structures, which work in single cells, may not work in stacks and vice versa.

Acknowledgment

The authors would like to thank the National Technology Agency TEKES and Academy of Finland for funding and VTT Technical Research Centre of Finland for providing flow-field plates for the experimental part of the work. The help and advice of D. Sc. Paavo Hassinen on structural mechanics are also gratefully acknowledged.

Nomenclature

- b = thickness (m)
- D = elasticity matrix (Pa)
- d = height (m)
- E = Young's modulus (Pa)
- I = coefficient of rigidity (m^4)
- $\mathbf{u}$ = deformation vector (m)
- u = x-directional deformation (m)
- v = y-directional deformation (m)
- w = z-directional deformation (m)

Greek Symbols

- γ_{ij} = shear strain in i,j-plane
- $\boldsymbol{\varepsilon}$ = strain tensor
- ε_i = i-directional normal strain
- υ = Poisson's ratio
- ρ = density ($kg\,m^{-3}$)
- $\boldsymbol{\sigma}$ = stress tensor (Pa)
- σ_i = i-directional normal stress (Pa)
- τ_{ij} = shear stress in i,j-plane (Pa)

References

[1] Ihonen, J., Mikkola, M., and Lindbergh, G., 2004, "Flooding of Gas Diffusion Backing in PEFCs," J. Electrochem. Soc., **151**(8), pp. A1152–A1161.
[2] Escribano, S., Blachot, J.-F., Ethève, J., Morin, A., and Mosdale, R., 2006, "Characterization of PEMFC Gas Diffusion Layer Properties," J. Power Sources, **156**(1), pp. 8–13.
[3] Lee, W., Ho, C.-H., Van Zee, J. W., and Murthy, M., 1999, "The Effects of Compression and Gas Diffusion Layers on the Performance of a PEM Fuel Cell," J. Power Sources, **84**(1), pp. 45–51.
[4] Evertz, J., and Günthart, M., 2003, "Structural Concepts for Lightweights and Cost-Effective end Plates for Fuel Cell Stacks," *Second European PEFC Forum*, Lucerne, Switzerland, Vol. 2, pp. 469–482.
[5] Lee, S.-J., Hsu, C.-D., and Huang, C.-H., 2005, "Analyses of the Fuel Cell Stack Assembly Pressure," J. Power Sources, **145**(2), pp. 353–361.
[6] Young, W. C., and Budynas, R. G., 2002, *Roark's Formulas for Stress and Strain*, 7th ed., McGraw-Hill, New York.
[7] Zienkiewicz, O. C., and Taylor, R. L., 2000, *Finite Element Method*, Vol. 1, 5th ed., Elsevier, New York.
[8] Ju, H., Meng, H., and Wang, C.-Y., 2005, "A Single-Phase, Non-Isothermal Model for PEM Fuel Cells," Int. J. Heat Mass Transfer, **48**(7), pp. 1303–1315.
[9] Grafoil data sheet at GrafTech, http://www.graftechaet.com/upload/GHA%20sheet%20properties.pdf, referred to on 26.10.2005.